scientific reports

Check for updates

OPEN

Hydrothermal extraction and physicochemical characterization of biogenic hydroxyapatite nanoparticles from buffalo waste bones for in vivo xenograft in experimental rats

Shada A. Alsharif[1], Mahmoud I. Badran[2], Moustafa H. Moustafa[2], Radwa A. Meshref[3] & Ehab I. Mohamed[2]✉

Hydroxyapatite (HA) can be used in odontology and orthopedic grafts to restore damaged bone due to its stable chemical characteristics, composition, and crystal structural affinity for human bone. A three-step hydrothermal method was used for the extraction of biogenic calcined HA from the buffalo waste bones at 700 °C (HA-700) and 1000 °C (HA-1000). Extracts were analyzed by thermogravimetric analysis, differential scanning calorimetry, X-ray fluorescence, X-ray diffraction, Fourier transform infrared spectroscopy, scanning electron microscopy, and in vivo examination of HA xenografts for femoral lesions in experimental rats. Crystallinity, purity, and morphology patterns showed that the HA main phase purity was 84.68% for HA-700 and 88.99% for HA-1000. Spherical HA nanoparticles were present for calcined HA-700 samples in the range 57–423 nm. Rats with critical bone lesions of 3 mm in diameter in the left femur treated with calcined HA-700 nanoparticles healed significantly ($p < 0.001$) faster than rats treated with HA-1000 or negative controls. These findings showed that spherical biogenic HA-700 NPs with a bud-like structure have the potential to stimulate both osteoconduction and bone remodeling, leading to greater bone formation potential in vivo. Thus, the calcined biogenic HA generated from buffalo waste bones may be a practical tool for biomedical applications.

Tissue and organ failure are critical concerns associated with longevity and a higher life expectancy due to increasing health expenditure and the continuous improvement of healthcare systems worldwide[1]. Tissue engineering involves creating, repairing, or replacing tissues and organs using biomaterials and biologically active molecules to restore, support, enhance function, or improve the quality of life of the patient[2,3]. Bioactive hydroxyapatite (HA), a calcium phosphate mineral, has been shown to stimulate bone restoration in both allografts and xenografts because of its stable chemical properties, composition, and crystal structural affinity for human bone[4,5]. However, hip and knee joint implants may fail due to many factors, including adverse body reactions, infection, pain, insufficient bonding, high stiffness, wear, improper placement, fractures, extensor mechanism failure, and aseptic loosening[6].

HA can be chemically synthesized using calcium and phosphorus chemical precursors, yet researchers have investigated and extracted biogenic HA from a variety of natural sources, primarily from biogenic mammalian resources like bovine, dromedary, porcine, and birds[7–9]. HA can also be extracted from marine or aquatic sources, such as fish scales and bones, shell sources, such as cockles, clams, eggs, and seashells, plants, algae, and mineral sources (e.g., limestone)[10]. These natural substrates have beneficial mechanical properties, biocompatibility, and biodegradability, making them affordable, nontoxic, and suitable for various biomedical applications[4–6].

[1]University College in Umluj, Tabuk University, Tabuk, Kingdom of Saudi Arabia. [2]Medical Biophysics Department, Medical Research Institute, Alexandria University, 165 El-Horreya Avenue, Alexandria 21561, Egypt. [3]Medical Equipment Technology Department, Faculty of Applied Health Sciences Technology, Pharos University, Alexandria, Egypt. ✉email: eimohamed@yahoo.com; ehab.abdo@alexu.edu.eg

Additionally, these unique chemical formulations could enhance the adsorptive treatment of heavy metal and dye contaminated wastewater in environmental applications[11]. Calcination, alkaline hydrolysis, precipitation, and hydrothermal are among the techniques employed to extract biogenic HA for biomedical applications[5,12,13]. However, the characteristics of biogenic HA, such as, calcium-to-phosphorus ratio, crystallinity, phase structure, particle sizes, and morphology, are highly dependent on the extraction method[7,10,14].

In the hydrothermal technique, the lysate of a substance is recrystallized at high temperature in a pressure autoclave to produce convection in the supersaturated state formation[13,14]. This procedure enables the extraction of highly-crystalline HA nanoparticles (NPs) from animal waste bones and calcinating them at high temperatures (normally in the range 600–1400 °C) to completely remove the organic matter and provide sterilized extracts[5–10,12–15].

X-ray diffraction (XRD) patterns of defatted, deproteinized, and calcined mammalian bones from humans, porcines, and bovines showed ordered crystal structures in the nanoscale range. The XRD patterns for ordered crystals are determined by the crystal size, with broad peaks for biogenic HA NPs extracts due to elastic and inelastic contributions[16]. Moreover, there exists a negative association between particle-specific surface area and temperature and a positive correlation with HA particle sizes and temperature, which may be the result of crystallization and agglomeration[10]. Furthermore, the biogenic HA extracts, unlike synthetic HA, have trace embedded impurities (e.g., Na^+, K^+, Zn^{2+}, Mg^{2+}, Si^{2+}, Ba^{2+}, F^-, PO_4^{3-}, and CO_3^{2-}) in the non-stoichiometric phase of the lattice, essential in xenograft for bone osteogenesis and remodeling in humans[10,15,16]. HA NPs are successfully used in biomedical realms, with viable implications in odontology and orthopedic grafts for fractured or damaged bone brought on by trauma, cancer, congenital, or other bone-related disorders[12,13]. Investigating the biological efficacy of biogenic HA as filling materials for critical size bone defect repair is still necessary as of this writing.

The aim of this study was to extract calcined biogenic HA from buffalo waste bones by a three-step hydrothermal approach, investigate its physicochemical properties, and evaluate its in vivo efficacy for treating critical-sized femoral lesions in experimental rats.

Materials and methods

Extraction of sterilized calcined buffalo HA powder

Buffalo (Bubalus *bubalis*) femur bones were obtained from healthy, mature sacrificed animals of three years old, sourced from the local slaughterhouse. The as-received bones from the slaughterhouse were thoroughly washed and cleaned at 100 °C (1:5, *w/v*, bone:water) for an hour to ease the removal of any organic substance from the bones[14,17]. 500 g of the clean bones were crushed into small pieces and placed in a 110 × 90 mm cylindrical autoclave at 130 °C and 1.5 atmo for 4 h to ease the removal of any organic residues and bone milling to achieve nanosized particles. The sterilized bones were further pulverized and sieved to a fine powder of uniform particle size. Finally, the raw bone powder was calcined and subjected to heat treatment in an electric box furnace under atmospheric conditions every 15 °C, till 700 and 1000 °C, at a heating rate of 5 °C/min and sintering for 2 h[17]. All samples were dried and labeled as raw bone (B-raw), calcined bone at 700 °C (HA-700), and calcined bone at 1000 °C (HA-1000) for subsequent in vivo testing on experimental rats.

Characterization of calcined buffalo HA extracts

Thermogravimetric analysis and differential scanning calorimetry (TGA/DSC)

The thermal breakdown and crystallization behavior of B-raw bone powders were studied from 25 to 900 °C in a nitrogen environment at a heating rate of 15 °C/min using a thermal analysis instrument (SDT Q600DSC-TGA, USA)[18–24]. Thermogravimetric analysis (TGA) was employed to record the weight loss changes in bone powder with increasing temperature. Differential scanning calorimetry (DSC) was used to quantitatively and qualitatively describe the physicochemical characteristics induced by endothermic and exothermic processes in bone powders as the temperature changed.

X-ray diffraction (XRD) analysis

An X-ray diffractometer (GNR, APD 2000 Pro, Italy) with a CuK target ($\lambda = 1.5406$ Å) and a voltage and current setting of 40 kV and 30 mA was used to examine the crystalline structure of all three HA powders, as described earlier[18,25,26]. Analysis of the XRD patterns of B-raw, HA-700, and HA-1000 samples was performed in the range $2\theta = 10°–80°$ with a step size of 0.05°. The standard diffraction data of the Joint Committee on Powder Diffraction Standards (JCPDS) reference 00-009-0432 for the HA phase was used for phase identification[28], while the crystallite size (X_c, nm) of the HA samples was calculated using Scherrer's equation:[29]

$$X_c = k\lambda/\beta Cos\theta \tag{1}$$

where k is a constant equal to 0.9, λ is the X-ray wavelength (1.54 Å), β is the full width at half maximum (FWHM, radians), and θ is the diffraction angle of the reflection plane at [002].

The sample crystallinity (D_c) was calculated using the Landi equation:[18]

$$D_c = 1 - V_{112/300}/I_{300} \tag{2}$$

where D_c is the crystallinity, $V_{112/300}$ is the intensity of the hollow between (112) and (300) peaks, and I_{300} is the intensity of the (300) diffraction peak of the biogenic HA powders.

X-ray fluorescence (XRF) spectroscopy analysis

A hand-held X-ray fluorescence (XRF) analyzer (Delta Premium, Olympus, Waltham, MA, USA), which can detect elements from ^{12}Mg through ^{83}Bi, was used to quantify elemental composition of B-raw buffalo femur

bone, as previously described[23,27–29]. The XRF was calibrated with a standard reference material before any measurements were made, and quality control was monitored using software[28]. Mineral content of B-raw samples was measured by scanning three locations on the femur midshaft for two minutes each. The percentage of elements that has measurement errors less than 5%, converted to mg/g units, was calculated by dividing the peak area of each element by the total area of all elements in the scan[27].

Fourier transform infrared (FTIR) spectroscopy analysis
The functional spectral groups for B-raw, HA-700, and HA-1000 powders were determined through Fourier-transform infrared (FTIR) spectroscopy using a Bruker tensor 27 IR spectrometer (Bruker Optik GmbH, Ettlingen, Deutschland), as detailed elsewhere[16,30–32]. The spectra were studied in the transmittance mode at a spectral resolution of 4/cm over the wave number range of 400–4000/cm.

Scanning electron microscopy (SEM)
The surface morphology and microstructure of B-raw, HA-700, and HA-1000 samples coated with a sputter coating evaporator (model: SPI Module, Sputter Carbon/Gold Coater) were analyzed using scanning electron microscopy (SEM; JEOL JSM 6510 lv, Japan) at 30 kV acceleration voltage[33,34].

In vivo study on experimental animals

Experimental design
Twelve adult albino rats were unilaterally lesioned at the left femur bone using a motorized drill and split into three equal experimental groups ($n = 4$). The animals received sham and xenograft HA treatments for 4 weeks. Negative controls with non-treated femoral lesions made up Group I; animals treated with HA-700 for their bone lesions made up Group II; and animals treated with HA-1000 for their bone lesions made up Group III.

Animals
Albino rats ($n = 12$) of two-month age and weighing 220–250 g at the start of the experiment were randomly divided into three equal groups ($n = 4$) with ad libitum drinking water and were kept on standard chow. The rats were housed in large rectangular cages ($49 \times 34 \times 16$ cm), each of which could house up to 4 adult rats, and each group was allowed to acclimate to the natural daylight cycle for one week. The Institutional Animal Care and Use Committee (IACUC #0121961521) approved the study's protocol before it began to ensure it followed the US National Institutes of Health's Guide for the Care and Use of Laboratory Animals (NIH publication no. 85-23, revised 1996)[35]. In addition, the procedures used and described here are consistent with the standards set forth by ARRIVE guidelines. The Ethics Committee of the Medical Research Institute, Alexandria University, Alexandria, Egypt, approved the study protocol.

Surgical procedure
Rats were anesthetized by injecting ketamine (50 mg/kg) and Lidocaine HCl (20 mg/ml) *i.p.* After the left femur was shaved, the periosteum and soft tissues were fixed, and a motorized drill was used to create a 3-mm-diameter lesion in the femur bone all the way to the medullary canal (as shown in Fig. 1A and B). Afterwards, xenograft treatment with HA-700 or HA-1000 was used to fill the femur bone lesion (Fig. 1C). After repositioning the skin and muscles, a 5-0 suture was used to close the wound (Fig. 1D).

Histology
After 4 weeks of sham and xenograft HA treatment, the rats were anesthetized once again, and a segment of the bone lesion region was removed from the left femurs. Afterwards, longitudinal serial sections 4–5 µm thick were cut from the samples with a microtome. The samples were then put in a 10% buffered formaldehyde solution for 24 h, and then they were decalcified in a 10% EDTA solution. Hematoxylin and Eosin (H&E) staining was used to analyze tissue sections under the microscope[36,37].

Blinding and masking
Four different researchers worked on each animal as follows: one researcher (MIB) assigned the animals to treatment groups and administered the sham and xenograft HA treatments following a randomization table. This researcher was the only one who knew which group received which treatment. A second investigator (MHM) administered the anesthesia, and a third (SAA, MIB, MHM) performed the surgery. The lesions and histological findings in the femur bones were finally evaluated by a fourth investigator (RAM, EIM), who was also blinded to the treatment.

Outcome measurements
After 4 weeks of sham and xenograft HA treatment, all the animals showed signs of healing, which was measured both in terms of the size of the inflicted lesion on the femur and its histological appearance under the microscope.

Statistical analysis
An analysis of variance (ANOVA) followed by Tukey's post hoc test of significance was used to compare the size of femur lesions between groups using the SPSS statistical package (Version 16; Chicago, IL, USA). The results were displayed in the form of means and standard deviations (SD). A p-value less than 0.05 was taken to show statistical significance.

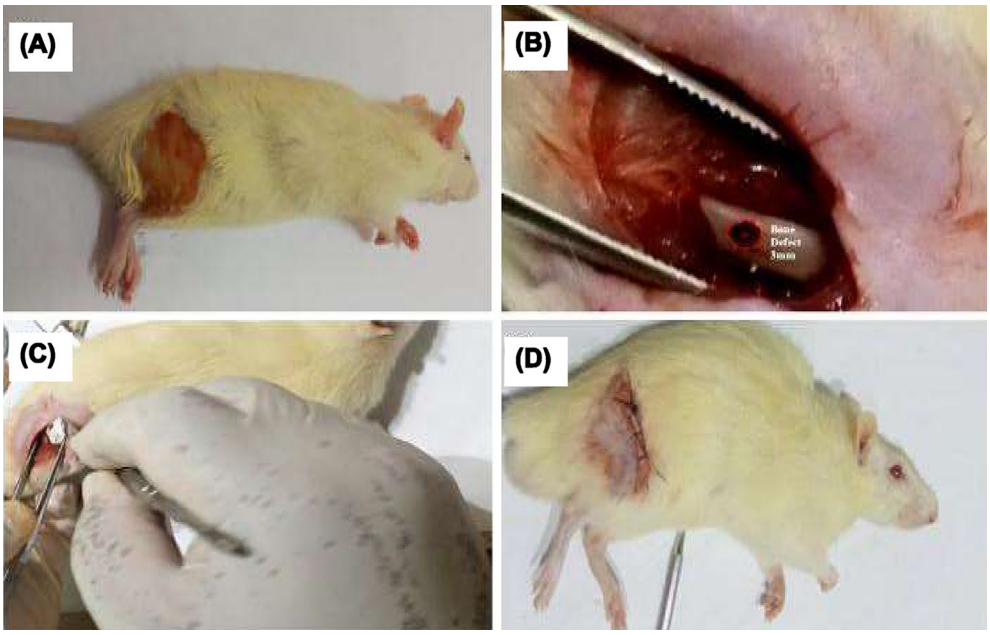

Figure 1. Surgical procedure showing an anesthetized rat with left femur shaved (**A**), periosteum and soft tissues fixed, and a 3-mm-diameter lesion drilled into femur bone to medullary canal (**B**), xenograft treatment with HA-700 or HA-1000 used to fill femur bone lesion (**C**) and wound closed with 5-0 suture (**D**).

Results and discussion

The increasing annual demand for biogenic HA in healthcare is due primarily to the growing number of patients worldwide who require orthopedic treatment. In this study, biogenic HA was extracted from buffalo waste bones using a three-step hydrothermal method at varying temperatures. The following techniques were used to characterize and evaluate biogenic HA extracts for in vivo xenografts in experimental rats.

TGA/DSC analysis

Derivative thermogravimetric analysis (DTGA), TGA, and DSC curves of B-raw bone powder sample decomposition due to temperature are shown in Fig. 2. Table 1 shows the DTGA temperature intervals, weight loss percentage, maximum decomposition peak temperature, and sample residues after combustion. Weight loss was initially seen in the range 38.66–169.57 °C of the DSC endothermic peaks due to the release of absorbed water and moisture content, accounting for 7.58% of the total mass with the maximum DTGA at 64 °C (Fig. 2A)[18,19]. A further 28.31% of the total mass is lost between 178.54 and 576.67 °C, which is characterized by a DTGA peak at 338.6 °C and a TGA sharp slope change (Fig. 2A and B), due to the combustion of bone's organic components

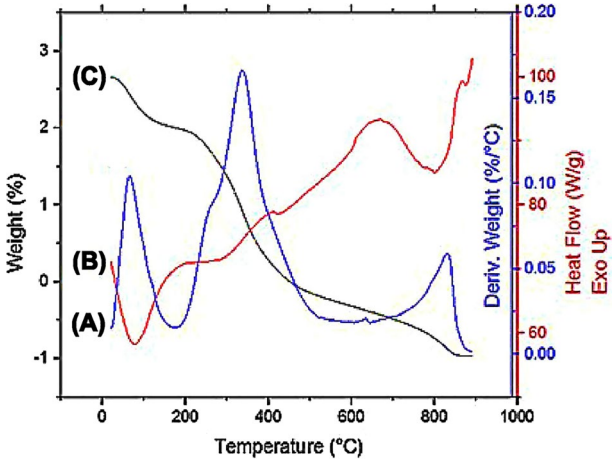

Figure 2. Derivative thermogravimetric analysis (DTGA) (**A**), thermogravimetric analysis (TGA) (**B**), and differential scanning calorimetry (DSC) (**C**) curves illustrating the temperature behavior for B-raw bone powder samples.

Temperature interval (°C)	DTGA peak temperature (°C)	Weight loss (wt.%)			Residue (wt.%)
		H_2O	Collagen	CO_3^{2-}	
38.66–169.57	64.0	7.58			
178.54–576.67	338.6		28.31		56.39
585.63–883.33	830.0			7.27	

Table 1. Temperature interval, maximum decomposition peak temperature, weight loss, and weight residue of bone powders by differential thermogravimetric analysis (DTGA).

including collagen polymer fibrils, which triggers the exothermic HA recrystallization process[20–22]. The final weight loss seen in the range 585.63–883.33 °C, accounting for 7.27% of the total mass with a maximum DTGA at 830 °C (Fig. 2A), corresponds to the endothermic peak in the TGA curve at 700 °C (Fig. 2B), owing to the slow elimination of the CO_3^{2-} ions from the HA lattice[31,32]. These observations are consistent with those of the subsequent FTIR spectroscopy analysis, which confirms the crystallization of B-raw bone powders and the loss of CO_3^{2-} groups due to high temperatures.

According to reports, thermal decarbonation commonly occurs between 400 and 600 °C in air and between 500 and 890 °C in a nitrogen environment[23]. No substantial weight loss related to the CO_3^{2-} decrease in the DTGA curve (Fig. 2A) was observed between 583 and 700 °C; this loss only becomes significant at 750 °C or higher[38], reflecting thermal stability. In line with earlier studies, raw bone powder calcined at 700 °C gives the best thermal stability and avoids the sintering effect under drastic changes in temperature for the extraction of HA[37,39]. Further temperature increases from 830 to 1000 °C result in minimal weight loss (~ 0.45%, DSC curve Fig. 2C) suggesting that HA crystals have formed entirely at that point.

XRD analysis

Crystallographic structure and phase purity of raw and calcined HA samples extracted at 700 °C and 1000 °C are shown by XRD patterns in Fig. 3. B-raw samples showed broad and poorly defined peaks at 2θ values of 25.85, 31.79, 39.83, and 46.74, respectively, which could not be reliably identified due to the presence of any leftover organic components as well as from the elastic and inelastic dispersion of the HA NPs crystals (Fig. 3A)[9,16]. The characteristic diffraction peaks of calcined HA-700 samples (Fig. 3B) found at $2\theta = 25.78$, 31.79, 32.21, 32.91, 34.01, 39.83, 46.74, 49.54, and 52.12, respectively, are well matched with the standard reference of the JCPDS 00-009-0432 for the HA phase[25]. The crystallite size (X_c) of HA-700 samples was 44.84 nm, with an 84.68% crystallinity (D_c), based on the diffraction peak at $2\theta = 25.78$ corresponding to the reflection plane [002]. Crystal size increased to 55.74 nm, and crystallinity increased to 88.99%, as shown by the narrower and sharper diffraction peaks of HA-1000 samples (Fig. 3C). In a similar earlier study, calcination was shown to increase the size of the crystals from nano to microscale and decrease the FWHM value, neither of which is directly associated with an improvement in crystalline quality[16,40]. Moreover, we did not observe any structural transformations or signs of secondary phases in the HA-700 and HA-1000 samples into beta-tricalcium phosphate (β-TCP) or calcium oxide (CaO), neither by hydrothermal treatment nor by calcination.

The FWHM and computed X_c at the diffraction peak $2\theta = 25.78$, which corresponds to the reflection plane [002], for B-raw, HA-700, and HA-1000 bone samples are shown in Fig. 3D and E. The higher FWHM value of 0.40 rad was associated with an X_c of 20.37 nm for B-raw samples. In similar studies, it was argued that the well-ordered and nanometric nature of biogenic HA nanocrystals from porcine origin resulted in broad XRD peaks, high FWHM values[16,40,41], and crystallite size of comparable values (i.e., 22 nm)[42]. After the calcination, the values of FMWH dramatically decreased, which was responsible for an increase in the X_c for HA-700 and HA-1000 (i.e., 44.84 and 55.74 nm, respectively). Evidence from XRD peaks and a similar decrease in the FWHM suggests that crystal growth is initiated during the calcination process of biogenic bovine HA[43].

XRF spectroscopy analysis

B-raw bone elements with measurement errors of less than 5% among locations on the femur midshaft were selected and shown in Table 2: *Ca*, *Cu*, *Fe*, *Mg*, *Mn*, *P*, *K*, *S*, *Si*, *Zn*, and *Ca*/*P* ratio. The values of *Ca*, *Fe*, *Mn*, *P*, and *Zn* for buffalo femur B-raw bones agree well with those for buffalo humerus bones by Buddhachat et al.[27], who employed the same technique for studying elemental composition in horns, teeth, and humeral bones of 14 different species, including humans, pigs, sheep, and buffalo. Moreover, the *Ca*/*P* ratio for buffalo femur B-raw bones was similar to that for humerus buffalo bones by the same group (i.e., 3.85 ± 0.05 vs. 3.70 ± 0.12, respectively)[27]. Furthermore, the values of *Ca*, *P*, *K*, and other bone minerals as well as the *Ca*/*P* ratio were similar to qualitative XRF elemental analysis in cow femur bones by Akindoyo et al.[23], and recent findings by Yılmaz et al.[44], in adult male and female guinea pigs.

FTIR spectroscopy analysis

The main functional ions PO_4^{3-}, CO_3^{2-}, and OH^-, water molecules (H_2O), and organic matrix of extracted bone samples as detected by the FTIR spectroscopy, in comparison with earlier similar studies[16,45–51], are shown in Table 3 and Fig. 4. B-raw samples showed a wide absorption band of organic components (collagen) at 2860.50 and 2921.43/cm (Fig. 4A), corresponding to the *C*–*H* symmetrical and asymmetrical stretching vibrational modes[16,50,51]. After calcination, PO_4^{3-} characteristic vibrational modes corresponding to the mineral bone

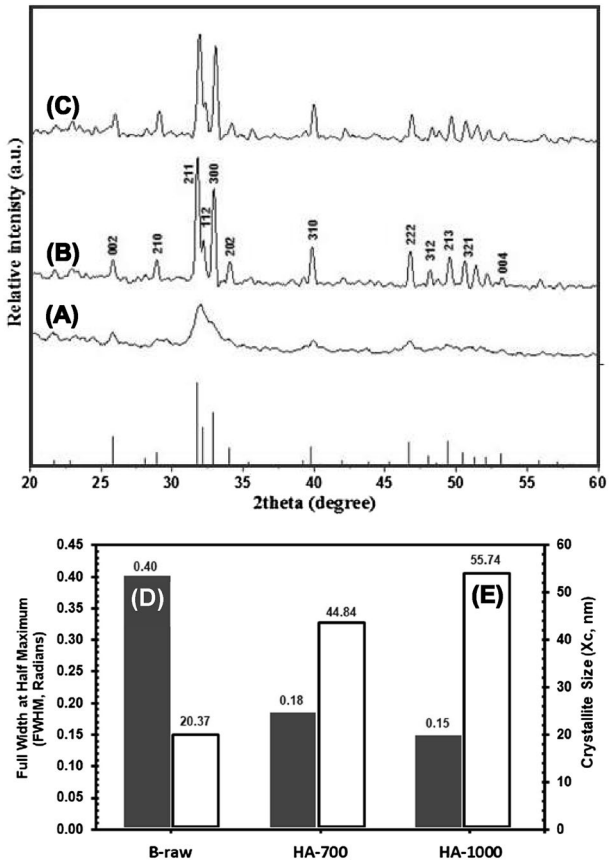

Figure 3. X-ray diffraction (XRD) patterns of B-raw (**A**), calcined HA-700 (**B**), and calcined HA-1000 (**C**) bone samples. Full width at half maximum (FWHM, radians) (**D**) and crystallite size (X_c, nm) (**E**) at the diffraction peak $2\theta = 25.78$ corresponding to the reflection plane [002] for each of the three bone samples using Scherrer's Eq. (1).

Mineral	Concentration (mg/g)
Calcium (*Ca*)	239.46 ± 20.22
Copper (*Cu*)	0.04 ± 0.02
Iron (*Fe*)	3.65 ± 1.61
Magnesium (*Mg*)	24.14 ± 2.39
Manganese (*Mn*)	0.39 ± 0.25
Phosphorus (*P*)	62.34 ± 12.55
Potassium (*K*)	4.98 ± 1.58
Sulphur (*S*)	1.74 ± 0.46
Selenium (*Se*)	4.97 ± 0.83
Zinc (*Zn*)	0.28 ± 0.11

Table 2. Elemental mineral content of buffalo B-raw femur bone by X-ray fluorescence (XRF) spectroscopy analysis.

component were present at 989.55/cm symmetric stretching (ν_1)[46], 1089.63/cm asymmetric stretching (ν_3)[45,46,48], 561.09, and bending 607.58/cm (ν_4)[48], as shown in Fig. 4B. The CO_3^{2-} group was present in and outside the HA-700 lattice, with characteristic spectral bands in the region 1404–1458/cm due to the doubly generated asymmetric stretching vibration (ν_3)[45,46,48,49]. The peak at 866.15/cm is believed to be due to the non-apatite environment's out-of-plane bending mode (ν_2)[45,49], which confirms the carbonation of HA-700 samples[31]. The CO_3^{2-} ions present in the lattice structure of HA-700 are known to be medically preferred because they enhance its biodegradability[2–6,12,13,17,19,22,24,36]. Adsorbed H_2O was conformed from the broad band centered at 3450.77/cm and an intense band at 1639.98/cm for HA-700 and at 3452.48/cm and 1639.90/cm for HA-1000 calcined samples (Fig. 4B and C), which are always present in bone-derived biological apatite[32,48,50]. Moreover, the characteristic stretching mode of the OH^- group faded in the spectra for all sintered samples due to overlap with the broad

Functional group	Vibration mode	Wavenumber (/cm)			Reference wavenumber (/cm)	References
		B-Raw	HA-700	HA-1000		
PO_4^{3-}	Bending ν_4 of PO_4^{3-} group	[608.32]	[561.09] [607.58]	[559.34] [605.63]	561	45
					562, 600	16
					565, 603	46
					568	47
					601	48
	Asymmetric stretching ν_3 of PO_4^{3-} group	[1084.37]	[1089.63]	[1087.82]	1043, 1091	46
					1087	45
					1091	48
	Symmetric stretching ν_1 of PO_4^{3-} group	[991.28]	[989.55]	[989.45]	961	45
					964	46
					993	46
CO_3^{2-}	Asymmetric stretching ν_3 of CO_3^{2-} group	[1407.74–1458.48]	[1404.00–1458.00]	1404.14–1460	1408–4158	49
					1450	45
					1459	48
					1458	46
	Out of plane bending ν_2 of CO_3^{2-} group	[866.15]	[865.64]	[866.00]	868	49
					878	45
OH^-	Bending mode of H_2O molecule	[1642.82]	[1639.98]	[1639.90]	1642	50
	Stretching vibrations of $O–H$ bonds in adsorbed water molecules	[3448.92]	[3450.77]	[3452.48]	3419	48
Collagen	$C–H$ and $N–H$ stretching modes	[2860.50] [2921.43]	–	–	2800–3400	51
					2854, 2925	16
					2885, 2925	50

Table 3. Band positions for B-raw, HA-700, and HA-1000 bone samples and reference band positions of earlier studies by Fourier transform infrared (FTIR) spectroscopy analysis.

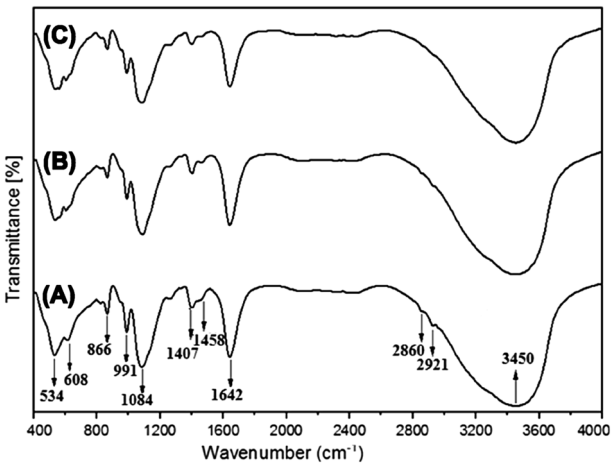

Figure 4. Fourier transform infrared (FTIR) analysis spectra of B-raw (**A**), calcined HA-700 (**B**), and calcined HA-1000 (**C**) bone samples.

H_2O absorption band centered at 3450/cm, also attributed to an increase in CO_3^{2-} substitution. Furthermore, calcined HA-1000 (Fig. 4C) showed a shift to lower wavelengths in the characteristic PO_4^{3-} group's band at 559.34, 605.63, and 1087.82/cm for the ν_3 and ν_4 vibrational modes[16,23,35–37]. Besides, the absorption bands at 1404–1460/cm of ν_3 $(CO_3)^2$ of reduced intensity showed that HA might lose CO_3^{2-} groups due to high temperatures up to 1000 °C[16,45,46,48,49].

SEM analysis

The SEM images of surface morphology for the raw and calcinated bone powder samples at a standard magnification of 30,000× are shown in Fig. 5. Like earlier studies[33,34], B-raw samples showed the presence of HA

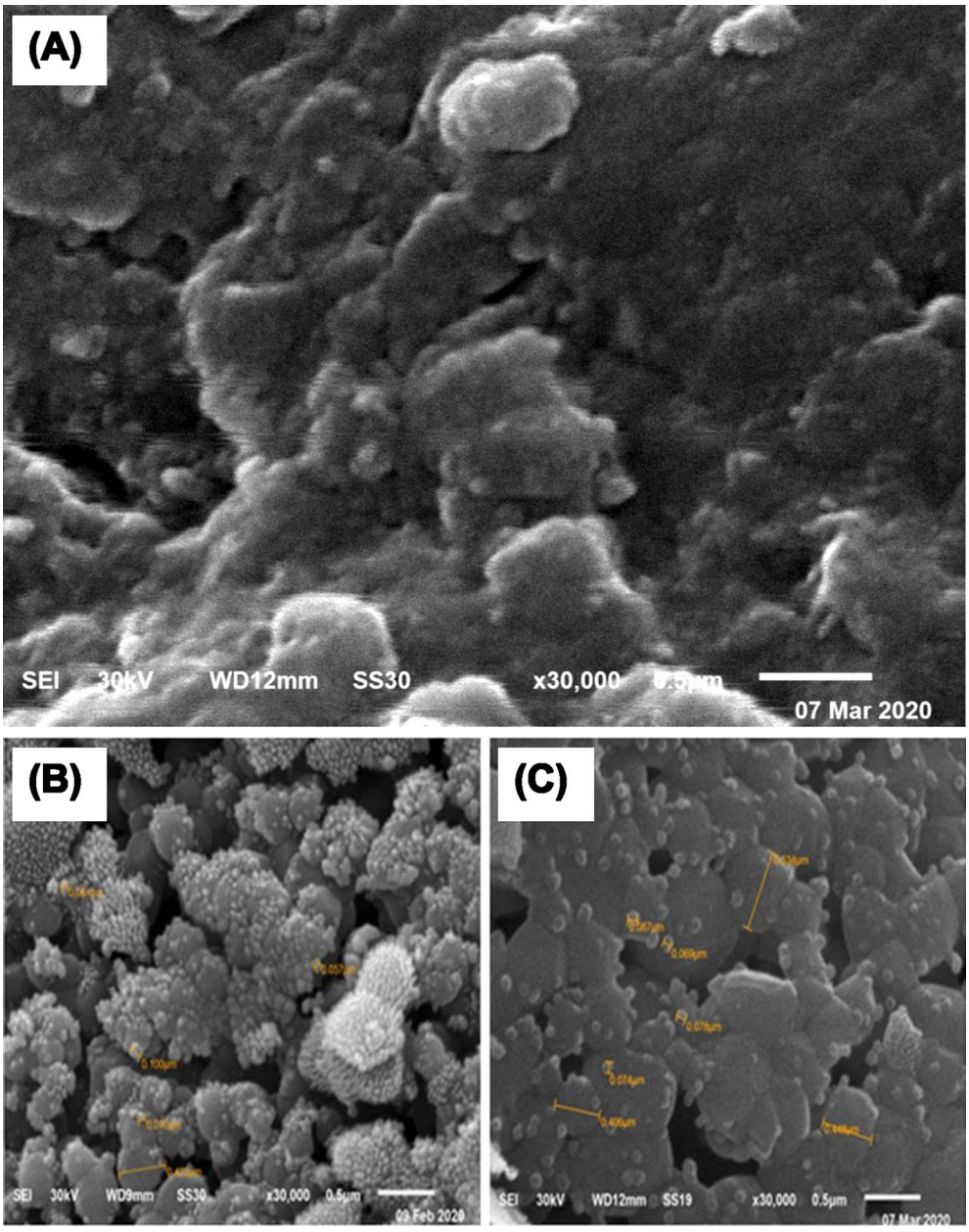

Figure 5. Scanning electron micrographs (SEM) of B-raw (**A**), calcined HA-700 (**B**), and calcined HA-1000 (**C**) bone samples at a standard magnification of 30,000×.

microparticles with an average size of 0.58 ± 0.47 µm of irregular shape and rough surface, together with organic components (Fig. 5A). Calcinated HA-700 samples showed a broad bud-like particle structure, with small spherical HA NPs of 57 nm on top of others of 423 nm size (Fig. 5B). Further higher calcination temperatures yielded aggregated particles of irregular shape in the range from 63 to 639 nm, as shown for HA-1000 samples in Fig. 5C. It has been pointed out earlier that after the calcination of raw bone powders at 700 °C, particles become more

regular and spherical in shape[34]. However, the majority of the HA extracted from mammalian bone exhibits irregular shapes, with some investigations showing the existence of flakes, rods, needles, and plate-like shapes[52–56].

During the calcination process, HA samples experience many changes, including crystallite size, shape, and crystalline quality, as well as dehydrogenation and Mg release at high temperatures[57]. It has recently been shown that the reduction in FWHM in biogenic bovine HA samples produced by controlled calcination at temperatures ranging from 400 to 720 °C is due to coalescence mechanisms directly related to crystallite size increase[58]. Furthermore, the XRF analysis in Table 2 shows that the B-raw bone samples have a significant concentration of Mg; thus, the nanosized spherical particles seen in SEM micrographs for the HA-700 and HA-1000 samples correspond to *MgO* in the calcined samples[42,58,59].

The bud-like structure of HA-700 NPs of two different sizes is remarkably original and has never been seen previously. Therefore, we suggest using the bud-like HA-700 NPs to treat critical-sized bone lesions. In the section that follows, it will be shown how treating critical-sized femoral lesions in a rat experimental model with in vivo xenografts may affect the biodegradability of bone during bone healing.

In vivo study on experimental animals

Photomicrographs at 200× of the left femur shaft of the negative control animals after four weeks showed large lesion sites filled with irregularly formed, unevenly stained, widely separated trabeculae of newly woven bone with mild inflammatory cell infiltration next to the lesion area (Fig. 6A). Unevenly stained bone trabeculae showing larger, densely grouped, and irregularly shaped osteocyte lacunae were also seen at 400× (Fig. 6B). Moreover, rat's left femur shaft treated with calcined HA-700 NPs after the same period showed lesion sites filled with new bone except for a few small, localized areas, small islands of cartilage, and an acidophilic normal compact bone (Fig. 6C) with normal osteocytes inside their lacunae (Fig. 6D). There were no inflammatory or foreign body reactions when using spherical calcined HA-700 NPs, which were osteoconductive and exhibited early biosorption, according to previous recent investigations, demonstrating healthy bone repair[36,37,60,61]. These results also lend credence to in vivo investigations showing that the substitution of CO_3^{2-} ions in the HA-700 NPs' lattice structure induces a favorable affinity for osteoblast cells, boosting cellular adhesion and collagen synthesis[62–65]. Furthermore, the rat's left femur shaft treated with HA-1000 particles after four weeks showed few widely trabeculae of woven bone, with mineralized and unmineralized areas, at the upper part of the lesion, with a partial bridging bon at the center at 200× (Fig. 6E). A persistent large lesion was also seen at 400× with trabecular bone, including a few osteocytes of irregular shape (Fig. 6F).

Based on these observations, we deduce that calcined HA-700 NPs significantly ($p < 0.001$) accelerated the healing of experimental rats with critical bone lesions of 3 mm in diameter in the left femur when compared to HA-1000 or negative controls. It has been shown earlier that HA-1000 particles had lower CO_3^{2-} ion contents, high crystallinity, and a large crystal size[66,67], which can explain their low resorption rate and poor integration with the newly formed woven bone in the lesion site during the healing process. Brandt et al.[68], previously reported that after 12 weeks of nanocrystalline HA implantation for bone repair, rabbit femoral bones showed bone formation, low degradation, and slow resorption. Clinical studies showed that HA could form direct physiological bonds with bone, resulting in good biocompatibility and no inflammatory response[69].

Conclusion

An efficient three-step hydrothermal approach was proposed to extract the pure crystalline phase of biogenic HA from buffalo waste bones, which was found to be stable throughout the range of temperatures investigated. The optimal temperature for the production of crystalline HA in the bone structure was reported to be 700 °C, which was sufficient for eliminating residual organic matter and enhancing the crystallinity of the HA phase. HA-700 extracts were characterized by their bud-like nonstoichiometric wide nano-range particle size and the presence of divalent PO_4^{3-} and CO_3^{2-} anions on the non-apatite hydrated layer. Despite their limited biodegradability, HA-700 NPs could form bone-like apatite coatings on their surfaces for better bone bonding, which is important in bone remodeling for in vivo xenograft treatment of critical sized femoral lesions in an experimental rat model. Thus, the study confirmed the effectiveness of manufacturing porous biogenic HA bodies for biomedical applications from buffalo waste bones using the hydrothermal technique.

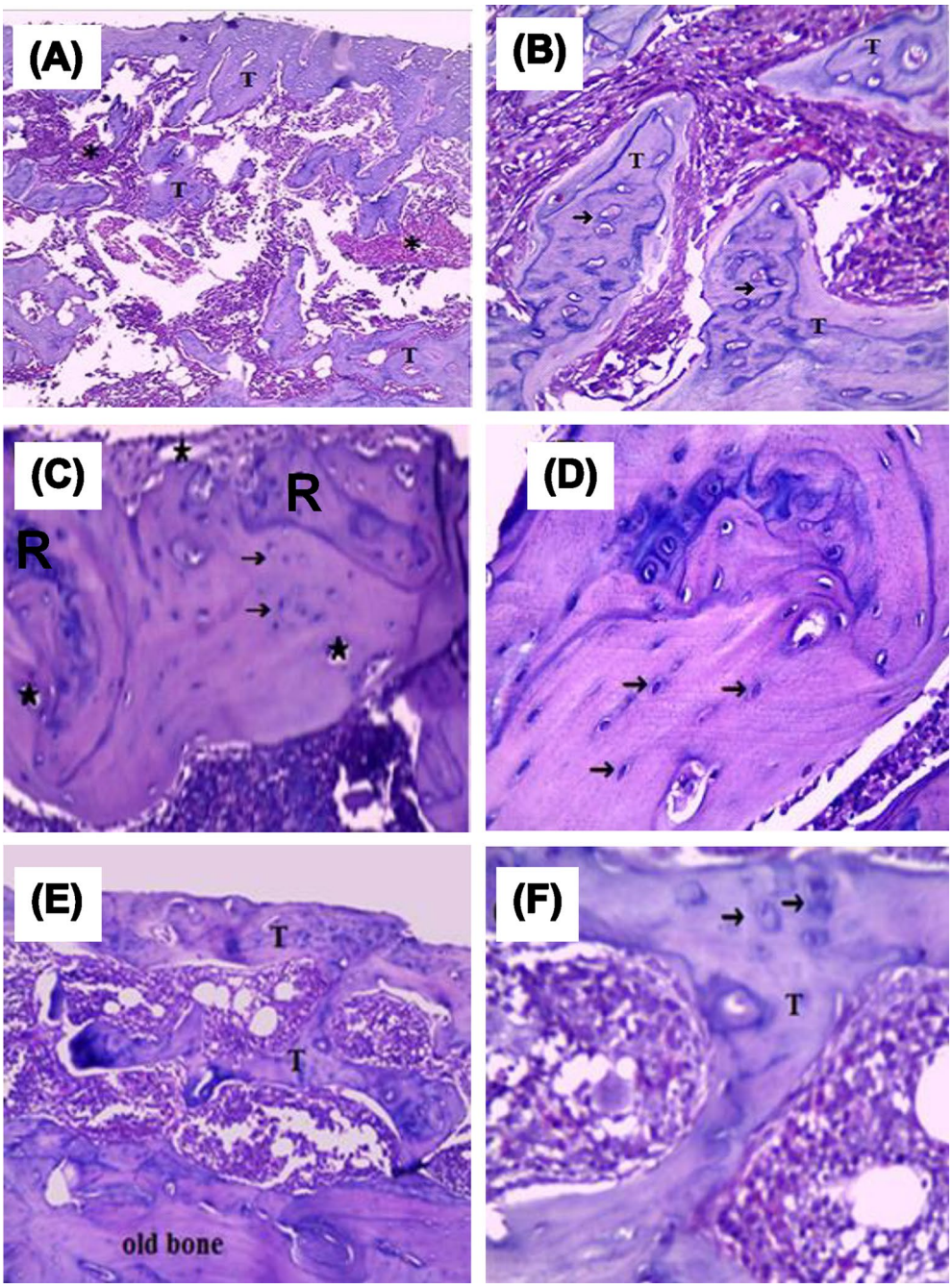

Figure 6. Photomicrographs of the left femur shaft of negative control animals ($n=4$) showing large lesion sites filled with irregularly formed unevenly stained widely separated trabeculae of woven bone (T) with mild inflammatory cell infiltration (*) (**A**); unevenly stained bone trabeculae exhibiting larger and more irregularly shaped lacunae (black arrow) at a higher magnification (**B**); treated animals ($n=4$) with HA-700 particles after four weeks showing lesions filled with new bone except for few small localized areas (*) and small islands of cartilage (R) (**C**); an acidophilic normal compact bone containing normal osteocytes inside their lacunae at a higher magnification (**D**); treated animals ($n=4$) with HA-1000 particles after 4 weeks showing a few widely separated trabecular bone (T) with a persistence large lesion (**E**); and trabecular bone containing few osteocytes with irregular shape at a higher magnification (**F**). (H&E Original magnification **A**, **C**, and **E** 200×; **B**, **D**, and **F** 400×).

Data and code availability

Metadata used and/or analyzed during the current study will be made available from the corresponding author on reasonable request.

Received: 18 April 2023; Accepted: 1 October 2023
Published online: 15 October 2023

References

1. Zarulli, V., Sopina, E., Toffolutti, V. & Lenart, A. Health care system efficiency and life expectancy: A 140-country study. *PLoS ONE* **16**, e0253450. https://doi.org/10.1371/journal.pone (2021).
2. Joyce, K., Fabra, G. T., Bozkurt, Y. & Pandit, A. Bioactive potential of natural biomaterials: Identification, retention and assessment of biological properties. *Sig. Trans. Targ. Ther.* **6**, 122. https://doi.org/10.1038/s41392-021-00512-8 (2021).
3. Rahmati, M., Pennisi, C. P., Budd, E., Mobasheri, A. & Mozafari, M. Biomaterials for regenerative medicine: Historical perspectives and current trends. *Adv. Exp. Med. Biol.* **1119**, 1–19. https://doi.org/10.1007/5584_2018_278 (2018).
4. Sobczak-Kupiec, A. *et al.* Review of the applications of biomedical compositions containing hydroxyapatite and collagen modified by bioactive components. *Mater. (Basel)* **14**, 2096. https://doi.org/10.3390/ma14092096 (2021).
5. Hussin, M.S.-F., Abdullah, H. Z., Idris, M. I. & Abdul Wahap, M. A. Extraction of natural hydroxyapatite for biomedical applications—a review. *Heliyon* **8**, e10356. https://doi.org/10.1016/j.heliyon.2022.e10356 (2022).
6. Kumar, S. *et al.* Nanotechnology-based biomaterials for orthopaedic applications: Recent advances and future prospects. *Mater. Sci. Eng. C.* **106**, 110154. https://doi.org/10.1016/j.msec.2019.110154 (2020).
7. Malla, K. P. *et al.* Extraction and characterization of novel natural hydroxyapatite bioceramic by thermal decomposition of waste ostrich bone. *Int. J. Biomater.* **2020**, 1690178. https://doi.org/10.1155/2020/1690178 (2020).
8. Ebrahimi, S., Stephen-Sipaut-Mohd-Nasri, C. & Bin Arshad, S. E. Hydrothermal synthesis of hydroxyapatite powders using response surface methodology (RSM). *PLoS One* **16**, e0251009. https://doi.org/10.1371/journal.pone.0251009 (2021).
9. Ghedjemis, A., Ayeche, R. & Benouadah, A. A comparative study on physicochemical properties of hydroxyapatite powder prepared from bovine and dromedary bone. *J. Aust. Ceram. Soc.* **58**, 607–616. https://doi.org/10.1007/s41779-022-00721-6 (2022).
10. Mohd Pu'ad, N. A. S., Koshy, P., Abdullah, H. Z., Idris, M. I. & Lee, T. C. Syntheses of hydroxyapatite from natural sources. *Heliyon* **5**, e01588. https://doi.org/10.1016/j.heliyon.2019.e01588 (2019).
11. Ghedjemis, A., Ayeche, R., Benouadah, A. & Feneniche, N. A new application of hydroxyapatite extracted from dromedary bone: Adsorptive removal of Congo red from aqueous solution. *Int. J. Appl. Ceram. Technol.* **18**(18), 590–597. https://doi.org/10.1111/ijac.13677 (2021).
12. Siddiqui, H. A., Pickering, K. L. & Mucalo, M. R. A review on the use of hydroxyapatite-carbonaceous structure composites in bone replacement materials for strengthening purposes. *Mater. (Basel)* **11**, 1813. https://doi.org/10.3390/ma11101813 (2018).
13. Ramesh, S. *et al.* Characterization of biogenic hydroxyapatite derived from animal bones for biomedical applications. *Ceram. Int.* **44**, 10525–10530. https://doi.org/10.1016/j.ceramint.2018.03.072 (2018).
14. Ma, G. Three common preparation methods of hydroxyapatite. *2019 IOP Conf. Ser. Mater. Sci. Eng.* **688**, 033057 (2019).
15. Pang, Y. & Bao, X. Influence of temperature, ripening time and calcination on the morphology and crystallinity of hydroxyapatite nanoparticles. *J. Eur. Ceram. Soc.* **23**, 1697–1704. https://doi.org/10.1016/S0955-2219(02)00413-2 (2003).
16. Londoño-Restrepo, S. M., Jeronimo-Cruz, R., Millán-Malo, B. M., Rivera-Muñoz, E. M. & Rodriguez-García, M. E. Effect of the nano crystal size on the x-ray diffraction patterns of biogenic hydroxyapatite from human, bovine, and porcine bones. *Sci. Rep.* **9**, 5915. https://doi.org/10.1038/s41598-019-42269-9 (2019).
17. Ho, Q.-P., Tao, T.-D., Huynh, L.-H. & Wang, M.-J. Biocomposite scaffold preparation from hydroxyapatite extracted from waste bovine bone. *Green. Proc. Synth.* **9**, 37–47. https://doi.org/10.1515/gps-2020-0005 (2020).
18. Resmim, C. M. *et al.* Study of physico-chemical properties and in vitro antimicrobial activity of hydroxyapatites obtained from bone calcination. *Prog. Biomat.* **8**, 1–9. https://doi.org/10.1007/s40204-018-0105-2 (2019).
19. Öksüz, K. E., Seyran-Kilinç, S. & Özer, A. Effect of calcination on microstructure development and properties of hydroxyapatite powders extracted from human and bovine bones. *Trans. Indian Ceram. Soc.* **78**, 41–45. https://doi.org/10.1080/0371750X.2019.1588170 (2019).
20. Ellingham, S., Thompson, T. & Islam, M. Thermogravimetric analysis of property changes and weight loss in incinerated bone. *Palaeog. Palaeocl. Palaeoeco.* **438**, 239–244. https://doi.org/10.1016/j.palaeo.2015.08.009 (2015).
21. Pramanik, S., Hanif, A. S. M., Pingguan-Murphy, B. & Abu-Osman, N. A. Morphological change of heat treated bovine bone: A comparative study. *Materials* **6**, 65–75. https://doi.org/10.3390/ma6010065 (2012).
22. Su, F. Y. *et al.* Deproteinization of cortical bone: Effects of different treatments. *Calcif. Tissue Int.* **103**, 554–566. https://doi.org/10.1007/s00223-018-0453-x (2018).
23. Akindoyo, J. O., Ghazali, S., Beg, M. D. H. & Jeyaratnam, N. Characterization and elemental quantification of natural hydroxyapatite produced from cow bone. *Chem. Eng. Tech.* **42**, 1805–1815. https://doi.org/10.1002/ceat.201800636 (2019).
24. Sakhno, Y., Iafisco, M. & Jaisi, D. Role of maturation temperature on structural substitution of carbonate in hydroxyapatite nanoparticles. *JOM* **73**, 1044–1052. https://doi.org/10.1007/s11837-021-04587-0 (2021).
25. Roopalakshmi, S., Ravishankar, R., Belaldavar, S., Prasad, R. G. S. V. & Phani, A. R. Investigation of structural and morphological characteristic of hydroxyapatite synthesized by sol-gel process. *Mater. Today: Proc.* **4**, 12026–12031. https://doi.org/10.1016/j.matpr.2017.09.126 (2017).
26. El Hadad, A. A. *et al.* Biocompatibility and corrosion protection behaviour of hydroxyapatite sol-gel-derived coatings on Ti6Al4V alloy. *Mater. (Basel)* **10**, 94. https://doi.org/10.3390/ma10020094 (2017).
27. Buddhachat, K. *et al.* Elemental analysis of bone, teeth, horn and antler in different animal species using non-invasive handheld X-ray fluorescence. *PloS One* **11**, e0155458. https://doi.org/10.1371/journal.pone.0155458 (2016).
28. Nganvongpanit, K. *et al.* Determining comparative elemental profile using handheld X-ray fluorescence in humans, elephants, dogs, and dolphins: Preliminary study for species identification. *Forens. Sci. Int.* **263**, 101–106. https://doi.org/10.1016/j.forsciint.2016.03.056 (2016).
29. Zdral, S., Monge Calleja, Á. M., Catarino, L., Curate, F. & Santos, A. L. Elemental composition in female dry femora using portable X-ray fluorescence (pXRF): Association with age and osteoporosis. *Calcif. Tissue Int.* **109**, 231–240. https://doi.org/10.1007/s00223-021-00840-5 (2021).
30. Su, K. Y. & Lee, W. L. Fourier transform infrared spectroscopy as a cancer screening and diagnostic tool: A review and prospects. *Cancers (Basel)* **12**, 115. https://doi.org/10.3390/cancers12010115 (2020).
31. Fleet, M. E., Liu, X. & Liu, X. Orientation of channel carbonate ions in apatite: Effect of pressure and composition. *Am. Mineral.* **96**, 1148–1157. https://doi.org/10.2138/am.2011.3683 (2011).
32. Liu, Q., Pan, H., Chen, Z. & Matinlinna, J. P. Insight into bone-derived biological apatite: Ultrastructure and effect of thermal treatment. *Biomed. Res. Int.* **2015**, 601025. https://doi.org/10.1155/2015/601025 (2015).
33. Hammood, A. S., Hassan, S. S. & Alkhafagy, M. T. Access to optimal calcination temperature for nanoparticles synthesis from hydroxyapatite bovine femur bone waste. *Nano. Biom. Eng.* **3**, 228–235. https://doi.org/10.5101/NBE.V9I3.P228-235 (2017).
34. Kuśnieruk, S. *et al.* Influence of hydrothermal synthesis parameters on the properties of hydroxyapatite nanoparticles. *Beilstein. J. Nanotechnol.* **7**, 1586–1601. https://doi.org/10.3762/bjnano.7.153 (2016).
35. Wang, X. *et al.* Ulinastatin protects against acute kidney injury in infant piglets model undergoing surgery on hypothermic low-flow cardiopulmonary bypass. *PLOS ONE* **10**, e0144516. https://doi.org/10.1371/journal.pone.0144516 (2015).

36. Calasans-Maia, M. D. *et al.* Cytocompatibility and biocompatibility of nanostructured carbonated hydroxyapatite spheres for bone repair. *J. Appl. Oral. Sci.* **23**, 599–608. https://doi.org/10.1590/1678-775720150122 (2015).
37. Barakat, N. A. M. *et al.* Physiochemical characterizations of hydroxyapatite extracted from bovine bones by three different methods: Extraction of biologically desirable HAp. *Mater. Sci. Eng. C* **28**, 1381–1387. https://doi.org/10.1016/j.msec.2008.03.003 (2008).
38. Odusote, J. K., Danyuo, Y., Baruwa, A. D. & Azeez, A. A. Synthesis and characterization of hydroxyapatite from bovine bone for production of dental implants. *J. App. Biomat. Fun. Mater.* **17**, 2280800019836829. https://doi.org/10.1177/2280800019836829 (2019).
39. Garskaite, E. *et al.* Effect of processing conditions on the crystallinity and structure of carbonated calcium hydroxyapatite (CHAp). *Cryst. Eng. Commun.* **16**, 3950–3959. https://doi.org/10.1039/c4ce00119b (2014).
40. Castillo-Paz, A. M., Londoño-Restrepo, S. M., Tirado-Mejía, L., Mondragón, M. A. & Rodríguez-García, M. E. Nano to micro size transition of hydroxyapatite in porcine bone during heat treatment with low heating rates. *Progr. Nat. Sci. Mater. Int.* **30**(4), 494–501. https://doi.org/10.1016/j.pnsc.2020.06.005 (2020).
41. Londoño-Restrepo, S. M., Herrera-Lara, M., Bernal-Alvarez, L. R., Rivera-Muñoz, E. M. & Rodriguez-García, M. E. In-situ XRD study of the crystal size transition of hydroxyapatite from swine bone. *Ceram. Int.* **46**, 24454–24461 (2020).
42. Zubieta-Otero, L. F. & Rodriguez-Garcia, M. E. Obtention and characterization of nano bio-hydroxyapatite particles by combined hydrothermal alkaline and ultrasonic wet milling methods. *Next Mater.* **1**, 100019. https://doi.org/10.1016/j.nxmate.2023.100019 (2023).
43. Londoño-Restrepo, S., Jeronimo-Cruz, R., Rubio-Rosas, E. & Rodriguez-García, M. The effect of cyclic heat treatment on the physicochemical properties of bio hydroxyapatite from bovine bone. *J. Mater. Sci. Mater. Med.* **29**, 1–15. https://doi.org/10.1007/s10856-018-6061-5 (2018).
44. Yılmaz, Y. *et al.* Physical and chemical characterization of the femur during and after the body development period in male and female guinea pigs. *Anim. Sci. J.* **94**, e13848. https://doi.org/10.1111/asj.13848 (2023).
45. Sossa, P. A. F., Giraldo, B. S., Garcia, B. C. G., Parra, E. R. & Arango, P. J. A. Comparative study between natural and synthetic hydroxyapatite: Structural, morphological and bioactivity properties. *Matér. (Rio de Janeir.)* **23**, e12217. https://doi.org/10.1590/s1517-707620180004.0551 (2018).
46. Raya, I., Mayasari, E., Yahya, A., Syahrul, M. & Latunra, A. I. Synthesis and characterizations of calcium hydroxyapatite derived from crabs shells (*Portunus pelagicus*) and its potency in safeguard against to dental demineralizations. *Int. J. Biomat.* **2015**, 469176. https://doi.org/10.1155/2015/469176 (2015).
47. do-Desterro, F. P., Sader, M. S., Soares, G. D. & Vidigal, G. M. Can inorganic bovine bone grafts present distinct properties?. *Braz. Dent. J.* **25**, 282–288. https://doi.org/10.1590/0103-6440201300067 (2014).
48. Heidari, F. *et al.* Investigation of mechanical properties of natural hydroxyapatite samples prepared by cold isostatic pressing method. *J. Alloys Comp.* **693**, 1150–1156. https://doi.org/10.1016/j.jallcom.2016.10.081 (2017).
49. Ressler, A. *et al.* Multiphase zinc and magnesium mono-substituted calcium phosphates derived from cuttlefish bone: A multi-functional biomaterials. *Ceram. Int.* **49**(7), 11005–11017. https://doi.org/10.1016/j.ceramint.2022.11.295 (2023).
50. Zubieta-Otero, L. F., Londoño-Restrepo, S. M., Lopez-Chavez, G., Hernandez-Becerra, E. & Rodriguez-Garcia, M. E. Comparative study of physicochemical properties of bio-hydroxyapatite with commercial samples. *Mater. Chem. Phys.* **259**, 124201. https://doi.org/10.1016/j.matchemphys.2020.124201 (2021).
51. Figueiredo, M. *et al.* Effect of the calcination temperature on the composition and microstructure of hydroxyapatite derived from human and animal bone. *Ceram. Int.* **36**, 2383–2393. https://doi.org/10.1016/j.ceramint.2010.07.016 (2010).
52. Janus, A. M., Faryna, M., Haberko, K., Rakowska, A. & Panz, T. Chemical and microstructural characterization of natural hydroxyapatite derived from pig bones. *Microchim. Acta* **161**, 349–353. https://doi.org/10.1007/s00604-007-0864-2 (2008).
53. Barakat, N. A., Khil, M. S., Omran, A., Sheikh, F. A. & Kim, H. Y. Extraction of pure natural hydroxyapatite from the bovine bones bio waste by three different methods. *J. Mater. Process. Technol.* **209**, 3408–3415. https://doi.org/10.1016/j.jmatprotec.2008.07.040 (2009).
54. Ofudje, E. A. *et al.* Synthesis of organic derived hydroxyapatite scaffold from pig bone waste for tissue engineering applications. *Adv. Powd. Technol.* **29**, 1–8. https://doi.org/10.1016/j.apt.2017.09.008 (2018).
55. Ruksudjarit, A., Pengpat, K., Rujijanagul, G. & Tunkasiri, T. Synthesis and characterization of nanocrystalline hydroxyapatite from natural bovine bone. *Curr. Appl. Phys.* **8**, 270–272. https://doi.org/10.1016/j.cap.2007.10.076 (2008).
56. Haberko, K. *et al.* Natural hydroxyapatite—its behaviour during heat treatment. *J. Eur. Ceram. Soc.* **26**, 537–542. https://doi.org/10.1016/j.jeurceramsoc.2005.07.033 (2006).
57. Ramirez-Gutierrez, C., Londoño-Restrepo, S., Del Real, A., Mondragón, M. & Rodriguez-García, M. Effect of the temperature and sintering time on the thermal, structural, morphological, and vibrational properties of hydroxyapatite derived from pig bone. *Ceram. Int.* **43**, 7552–7559. https://doi.org/10.1016/j.ceramint.2017.03.046 (2017).
58. Cañon-Davila, D. F. *et al.* Study of the coalescence phenomena in biogenic nano-hydroxyapatite produced by controlled calcination processes at low temperature. *Ceram. Int.* **49**, 17524–17533. https://doi.org/10.1016/j.ceramint.2023.02.119 (2023).
59. Bahrololoom, M. E., Javidi, M., Javadpour, S. & Ma, J. Characterisation of natural hydroxyapatite extracted from bovine cortical bone ash. *J. Ceram. Process. Res.* **10**, 129–138 (2009).
60. El-Meliegy, E., Abu-Elsaad, N. I., El-Kady, A. M. & Ibrahim, M. A. Improvement of physico-chemical properties of dextran-chitosan composite scaffolds by addition of nano-hydroxyapatite. *Sci. Rep.* **8**, 12180. https://doi.org/10.1038/s41598-018-30720-2 (2018).
61. Edén, M. Structure and formation of amorphous calcium phosphate and its role as surface layer of nanocrystalline apatite: Implications for bone mineralization. *Materialia* **17**, 101107. https://doi.org/10.1016/j.mtla.2021.101107 (2021).
62. Rupani, A. *et al.* Osteoblast activity on carbonated hydroxyapatite. *J. Biomed Mater. Res. Part A* **100**, 1089–1096. https://doi.org/10.1002/jbm.a.34037 (2012).
63. Khotib, J. *et al.* Signaling pathway and transcriptional regulation in osteoblasts during bone healing: Direct involvement of hydroxyapatite as a biomaterial. *Pharmaceuticals* **14**(7), 615. https://doi.org/10.3390/ph14070615 (2021).
64. Pupilli, F. *et al.* Design strategies and biomimetic approaches for calcium phosphate scaffolds in bone tissue regeneration. *Biomimetics* **7**, 112. https://doi.org/10.3390/biomimetics7030112 (2022).
65. Gani, M. A., Budiatin, A. S., Shinta, D. W., Ardianto, C. & Khotib, J. Bovine hydroxyapatite-based scaffold accelerated the inflammatory phase and bone growth in rats with bone defect. *J. Appl. Biomater. Fun. Mater.* **21**, 22808000221149190. https://doi.org/10.1177/22808000221149193 (2023).
66. Liu, Q. *et al.* Effect of thermal treatment on carbonated hydroxyapatite: Morphology, composition, crystal characteristics and solubility. *Ceram. Int.* **41**, 6149–6157. https://doi.org/10.1016/j.ceramint.2014.11.062 (2015).
67. Um, S.-H. & Rhee, S.-H. In vivo evaluations of hydroxyapatites with small and large grain sizes. *Adv. Appl. Ceram.* **118**, 484–490. https://doi.org/10.1080/17436753.2019.1667176 (2019).
68. Brandt, J. *et al.* Nanocrystalline hydroxyapatite for bone repair: An animal study. *J. Mater. Sci. Mater. Med.* **21**, 283–294. https://doi.org/10.1007/s10856-009-3859-1 (2010).
69. Jarcho, M. Calcium phosphate ceramics as hard tissue prosthetics. *Clin. Orthop. Relat. Res.* **157**, 259–278 (1981).

Acknowledgements
A patent 210/2021 titled "A Novel Extraction Method of Biological Hydroxyapatite Powder for Formulating Active Inorganic Nanoparticles for Biomedical Applications" was granted by the Academy of Scientific Research and Technology in Cairo, Egypt, and describes the three-step hydrothermal extraction procedure used to create hydroxyapatite nanoparticles from buffalo waste bones.

Author contributions
S.A.A. and M.I.B. contributed equally to the study. S.A.A.: investigation, XRF analysis, visualization, critical analysis, and writing—review and editing. M.I.B.: conceptualization, experimental design, methodology, carrying out measurements, formal analysis, and writing original draft. M.H.M.: methodology, data curation, formal analysis, visualization, and writing—review and editing. R.A.M.: methodology, data curation, formal analysis, visualization, and writing—review and editing. E.I.M.: conceptualization, experimental design, methodology, formal analysis, visualization, software, writing - original draft, and writing—review and editing. All authors have read and approved the final manuscript.

Funding
This research received no specific grant from public, commercial, or not-for-profit funding agencies.

Competing interests
The authors declare no competing interests.

Additional information
Correspondence and requests for materials should be addressed to E.I.M.

Reprints and permissions information is available at www.nature.com/reprints.

Publisher's note Springer Nature remains neutral with regard to jurisdictional claims in published maps and institutional affiliations.